

GRID EFFECT ON M823 BOMB AT TRANSONIC REGIME

José Jiménez-Varona¹, Gabriel Liaño¹

¹INTA, National Institute for Aerospace Technology, Torrejón de Ardoz, 28850 Madrid, Spain

Abstract

The flow field past an axisymmetric body configuration at high angles of attack is asymmetric, and unsteady. Projectiles, missiles and bombs are composed of an axisymmetric body with a fins set and/or strakes. At subsonic and transonic regimes, the flow may be asymmetric at certain angles of attack, due to instabilities at the tip nose region, amplified by the leeside vortex interaction with the rear fins. The role of grids in such cases is very decisive when numerical calculations are performed. Excessive irregularities in the tip nose region, due to a coarse and/or inaccurate definition of the tip, may lead to important differences of the calculated forces and moments when compared to experimental data. The grid role in terms of resultant forces and moments may be large at high angles of attack, where there are nonlinear effects, some of them due to spurious numerical effects. This effect may also be significant in rolling motion and on the derived Magnus forces and moments at high angles of attack.

Keywords: Aerodynamics, transonic, rolling, CFD, grids.

1. Introduction

Computational Fluid Dynamics (CFD) is nowadays a reliable tool for the characterization of the flow field past aircraft. Accurate aerodynamic coefficients can be computed with CFD codes, provided fine grids, high order methods and high level turbulence models are used. There are many CFD codes which implement Unsteady Reynolds Average Navier-Stokes (URANS) methods. These methods are mature and accurate for predicting the flows past certain configurations. However, the numerical simulation of the flow past an axisymmetric body at high angles of attack is still a challenging problem.

Many studies and experiments have demonstrated that at high angles of attack the flow past an axisymmetric body is asymmetric. There are non-zero side force and yawing moment. This side force may be of similar magnitude than the normal force in some cases. Moreover, there is a roll or orientation angle dependence of the pressure field. References [1-17] contain the results and conclusions of many investigators developed since the 80's of the past century to nowadays.

There are two main parameters which have a strong influence on this asymmetric flow pattern: the Mach number and Reynolds number. The asymmetric flow disappears when the cross-flow Mach number exceeds a certain value. Then, this phenomenon is basically a subsonic and transonic flow phenomenon. Regarding the Reynolds number, the side force is maximum at laminar and fully turbulent flow, while at critical Reynolds number is minimum [1-3].

This behavior led to many investigators to suggest that there is an instability of inviscid nature which makes the flow to achieve a bi-stable asymmetric flow pattern. At certain conditions of angle of attack, the symmetric flow pattern is unstable, and a small perturbation of the flow (inhomogeneous free stream, turbulence, etc.) produces one of two possible asymmetric stable states. This is called global instability or temporal instability [1, 5, 11, 17].

This instability is also related to the geometry of the axisymmetric body, where the tip geometry, the fineness ratio and the imperfections in terms of roughness or eccentricities, play an important role

[4-17].

The tip is very important. A study for bodies of low fineness ratio led to an empirical correlation between the angle of attack for onset of asymmetry and the tip nose angle [1], [5-6]. At angles of attack larger than this, the symmetric pair of vortices formed at leeside are modified by the "vortex crowding" phenomenon. An inviscid instability (global) occurs when one vortex moves away from the body and the other vortex moves underneath the first [5]. This angle is $\alpha_{onset} = 2 \cdot \delta_{nose}$ being δ_{nose} the semi-apex angle. Rounding the tip increases the effective tip nose angle. Then, blunting delays the angle of attack for onset of asymmetry.

Finally, geometrical irregularities are very important on the flow pattern. For example, roughness is of paramount importance. In words of B.L. Hunt "One of the most curious, fascinating and infuriating flow problems to have been encountered in recent years is the body side-force problem. This roll angle variation is one of the most perplexing features of the side-force problem" [6].

Many experiments in wind tunnel test did not reproduce repeatability of solutions. Modifications of the tip of the model led to different values of side forces. There is a strong roll angle dependence on the forces. This is detailed in reference [1]; a bi-stable pattern of the side force with roll angle was described. A negative or positive side force of similar magnitude were obtained when testing a smooth model, with a dimensionless roughness of $\frac{Ra}{D} = 5 \cdot 10^{-6}$. A second rough model was tested.

This model was the original one painted and mechanized to have pressure taps for pressure measurements. The result was a model with a dimensionless roughness of $Ra/D = 40 \cdot 10^{-6}$. The new tests captured a sinusoidal side force with roll (orientation) angle, with variations of up to 50% from one roll angle to other.

There is another very important consequence of this roughness effect on the global forces. The angle of attack for onset of asymmetry of the rough model reduces significantly compared to the angle of attack for onset of asymmetry for the smooth model. This is shown by Champigny [1-3] and Deane et al. [18] for an ogive-cylinder configuration at low Mach number. Several investigators have made similar wind tunnel tests with smooth and rough models, achieving the same behavior: a bi-stable pattern of the side force for the smooth model, and a sinusoidal side force for the rough model [12-15]. This important effect of micro-imperfections have led many investigators to perturb the tip nose or to add roughness. This has also been investigated numerically [12-17]. The way to investigate numerically this effect is to modify the configuration of the mesh surface by adding geometrical micro-imperfections or some kind of numerical roughness.

This is a second source of asymmetry. The dependence of the forces with the roll (orientation) angle are related with these geometrical asymmetries. The mechanism is defined as a convective or spatial instability [5, 11]. Bridges defines in reference [5] that a convective instability has the following characteristics: (i) an asymmetric-infinitesimal disposed disturbance is fixed near the tip and the resulting flow develops an asymmetric mean side force component, (ii) a minute change of the disturbance results in a finite change of the forces, (iii) when the disturbance is removed, the flow relaxes back to its original state. Bao-Feng Ma [11] defines the spatial (convective) instability as the cause for asymmetric vortices due to the geometric imperfections or perturbations.

Then, it can be concluded that at high angles of attack there may be asymmetric flow due to both temporal (global) and spatial (convective) instabilities. The different measurements of Champigny [1-3] and Deane *et al.* [18] for smooth and rough models remark this idea. The roll angle dependence of the side forces for the rough model tests, and the different polar curves ranging in angle of attack indicate the action of both instability mechanisms.

For a numerical study, attention must be paid to the grids, as meshes play a decisive role in numerical simulation. In this case, the effect of geometrical irregularities of the bodies can be measured in terms of departure of the surface grids from the ideal axisymmetric body, especially in the tip nose, which plays a decisive role for triggering a spatial instability, which may lead to roll (orientation) angle dependence of the forces. Additionally to the key problem of the grids, it may be necessary to make transient calculations, due to the flow at high angles of attack may be unstable. There is another key

question. Most of the turbulence models used in codes that use the Unsteady Reynolds Averaged Navier-Stokes equations (URANS) are overly dissipative and resolve only frequencies far lower than turbulent fluctuations. The reason is that they do not display the correct spectrum of turbulent scales, even if the numerical grid and the time step would be of sufficient resolution [19-23]. Then, the Scale Adaptive Simulation (SAS) method, implemented by Menter and Egorov [19-24] could be used in transient problems.

For dynamic studies, roll damping derivatives or Magnus force derivatives and pitch damping moment sum are needed to be computed numerically.

Rolling motion is the motion where a body flies at a constant pitch angle α with respect to the freestream velocity vector, while undergoing a constant angular rotation p about its longitudinal axis. An effect of this motion is the appearance of additional forces and moments, which add to the static forces and moments. Classical studies of the rotation of a body of revolution in crossflow led to the definition of the Magnus effect. This Magnus effect consists of the appearance of forces parallel and normal to the incoming flow when the body is rotating [25]. Nielsen, when studying the missile's motion, defines the Magnus forces and moments as those developing as a result of rolling at an angle of attack [26]. For missiles, the Magnus effect of the body is usually small compared to that of the fins. The classical approach considers the Magnus side force linear with the reduced roll rate and the angle of attack. This is a good approach for low angles of attack [26]. Using the Maple—Synge analysis, some researchers showed that there are in-plane and out-of-plane Magnus terms [27]. They developed a model of the non-linear forces in rolling motion. Liaño $et\ al.\ [28-29]\ used\ a$ strong non-linear model for the pitching moment to study the lateral motion of missiles. Therefore, for rolling motion at high angles of attack studies, a question that arises is the appearance of non-linear effects similar to those described in these references.

Concerning missiles and axisymmetric bodies, a question arises regarding the Magnus effect at high angles of attack, where the flow over an axisymmetric body is not symmetric, leading to a non-zero side force at zero spin rate [1, 5, 6, 16]. Additionally, the roughness induces a roll angle effect on the side and normal forces, and therefore on the moments [5-6]. Then, a prediction of the Magnus effect is difficult to assess.

In this paper, a study of the M823 bomb configuration at transonic flow conditions has been carried out. The effect of the grid on the force and moment coefficients calculations has been estimated. Experimental data given in some references were used for comparisons [30-31] at zero spin conditions. Then, rolling at different spin rates was calculated in order to estimate Magnus force and moment coefficients as well as rolling moment coefficient. The decisive role of the mesh will be remarked.

2. Reference case: M823 bomb configuration at transonic flow

A configuration of a classical bomb -the M823 bomb- composed by an axisymmetric body and a set of four fins is used for the calculations [30-31].

A sketch of the configuration is seen in Fig 1. The bomb has four freely spinning cruciform stabilizers. Two wind tunnel tests models were used for tests campaigns at several wind tunnels. These are 1:10 scale models of the baseline configuration. Details of the dimensions of the different parts that conform the baseline configuration are given in [30-31].

A body axis system is used. This reference system for the forces and moments is a non-rolled body axis system. The x-axis is the longitudinal axis of the body. The y and z axes are orthogonal to the x-axis and define a Cartesian coordinate system. In general, the origin is taken at the tip nose. For comparison of the moments with the experimental data, the origin of moments has been properly chosen; usually at the center of gravity defined in [30-31].

The maximum diameter of the body sections (*D*) is taken for defining the reference area. This diameter is also used for the reference length for the moments.

For comparisons at different roll (orientation) angles calculations, it is useful to compare the in-plane (defined by X-N axes) and out-of-plane (defined by N-S axes) forces. The transformation matrix is:

$$\begin{pmatrix} 1 & 0 & 0 \\ 0 & \cos\phi & -\sin\phi \\ 0 & \sin\phi & \cos\phi \end{pmatrix} \text{ and then, } C_{side} = C_y \cdot \cos\phi - C_z \cdot \sin\phi$$

$$C_{normal} = C_y \cdot \sin\phi + C_z \cdot \cos\phi$$

$$(1)$$

Similarly with the moments. The moment in X-direction is the rolling moment. The pitching moment is in the S-axis and the yawing-moment is in the N-axis.

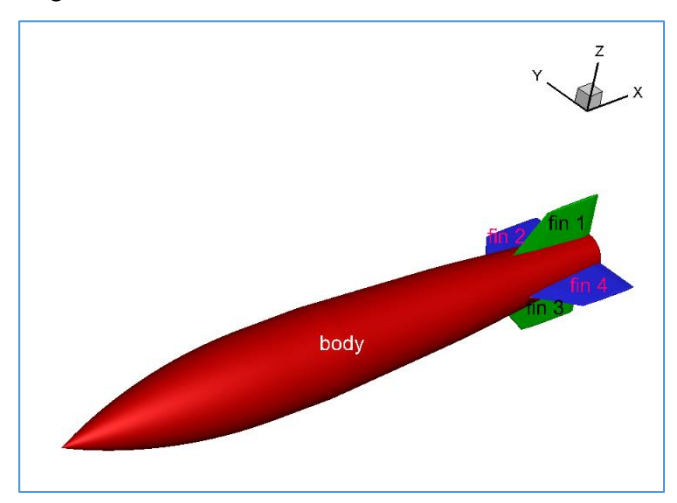


Figure 1 – Sketch of M823 bomb configuration.

For the computations, all the cases have been run in International Standard Atmosphere (ISA). The conditions are:

- Altitude h = 10000 m (Pressure = 26500 Pa, Temperature = 226 °K)
- Mach number (Ma) = 0.85

The Reynolds number is defined as $\operatorname{Re} = \frac{\rho_{\scriptscriptstyle \infty} \cdot \nu_{\scriptscriptstyle \infty} \cdot D}{\mu_{\scriptscriptstyle \infty}}$ being D the maximum diameter. For the baseline

configuration, this diameter is: D = 0.47625 m (18.75 inches). Then, as all the cases are run at the same altitude, the Reynolds number is $Re_{\infty} = 3.4 \times 10^6$.

The range of angle of attack is $\alpha = \{0, 30\}$ degrees. The wind tunnel tests were run at this range.

There is experimental information in reference [30] regarding tests at Naval Ordnance Laboratory (NOL) and at Aircraft Research Association (ARA) wind tunnels. For the case of NOL wind tunnel the

Reynolds number was $\text{Re}_D = 4.15 \times 10^6 \frac{1}{ft}$ at the case at Mach number $M_{\infty} = 0.85$. This corresponds -

taking into account the diameter of 1.875 inches- with a Reynolds number of $Re_{\infty} = 6.48 \times 10^5$. Then, the experimental data used for comparisons are obtained at a lower Reynolds number.

2.1 Grids

Several grids were generated for the computations. Some of them have been built up with internal procedures. These grids are hybrid unstructured meshes, formed by prismatic and tetrahedral cells. The concept of sliding mesh, very useful for rolling motion computations has been used for the grid generation [24]; close to the body a fine cylinder mesh is built such that it can move rotating around the longitudinal axis if calculations with a constant angular velocity are done. This cylinder may rotate with the correspondent body rotation whereas the outer cylinder remains fixed. The solution in the nearfield is obtained in a moving reference frame, while in the outer field an inertial reference frame is used. In the interface proper interpolation of the fluxes must be done (for details see reference [24]). This mesh can also be used for plunging or harmonic motion in angle of attack, although in this case this mesh has to be a dynamic mesh which deforms with the body movement. The pitch damping

moment coefficient $sum(C_{mq} + C_{m\dot{\alpha}})$ can be obtained with harmonic motion. A detail of this sliding mesh is given in Fig. 2.

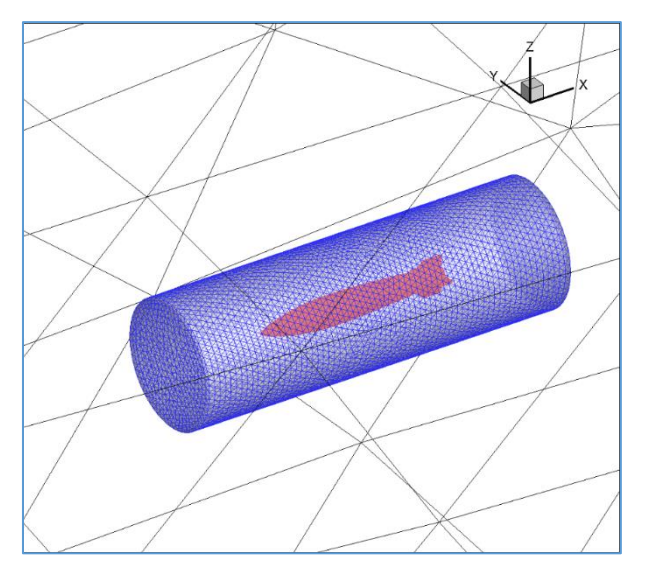


Figure 2 – Sliding mesh: inner cylinder.

This first grid was generated with internal procedures. This procedure of grid generation has led to important geometrical irregularities, particularly in the ogive region of the body. One way to overcome these geometrical irregularities, is a procedure to modify the surface grid points' position. The body is a body of revolution. Then, at each x-coordinate, all the grid points must fulfil a law, such that the radius is constant. The departure of the grid points from the ideal position gives a measure of the irregularity. Therefore, the new grid is generated after manipulation of the resultant surface grid points. An additional third grid was generated by using a different mesh generation procedure. This grid was not generated with the sliding grid concept in this case. It was coarser than the others. The CENTAUR® mesh generator was used. Again, a hybrid mesh, with prismatic layers and tetrahedral cells was built up.

A brief description of some features of the grids is shown in Table 1. The table contents are referred to the three grids which have been used for the computations.

Grid	Surface elements	Prismatic layers	Number of faces	Number of cells
Grid MU1	215840	48	32226602	13459149
Polished grid MU2	215840	48	32222496	13457096
Centaur grid MU3	106712	48	23362843	10539527

Table 1 – Features of the grids

The grid MU3 is coarser than the others. Particularly, the surface mesh is half the size of the surface meshes of the others. However, as it will be shown below, this mesh generator (CENTAUR® code) creates a surface mesh smoother and more symmetric than the other procedure does; particularly in the tip nose region. The effect on the solutions at high angles of attack conditions will be explained below.

2.2 Geometric irregularities of the surface meshes

The geometric irregularities, in terms of departure of the grid points from their ideal position, have been estimated for the three grids. This is not a measure of roughness. But, it gives a measure of the irregularity of the surface meshes of these grids. The effect on the solutions is significant, as it has been verified in other calculations at low subsonic flow.

2.2.1 Grids MU1 and MU2

A graphical view of the departure of the MU1 surface mesh from the ideal axisymmetric body, is seen in Fig. 3. This departure, defined as $diff(x_i)$, is plotted at every section. Only in the tip nose region (x-coordinate less than 0.1 m) the deviation is large. In the rest of the body, which is theoretically an axisymmetric body, there are deviations with average values close to 50 µm. This can be an important amount in terms of roughness. Therefore, it can be concluded that this mesh resembles not only a rough test model, but also a non-symmetric configuration; at least on the tip nose region.

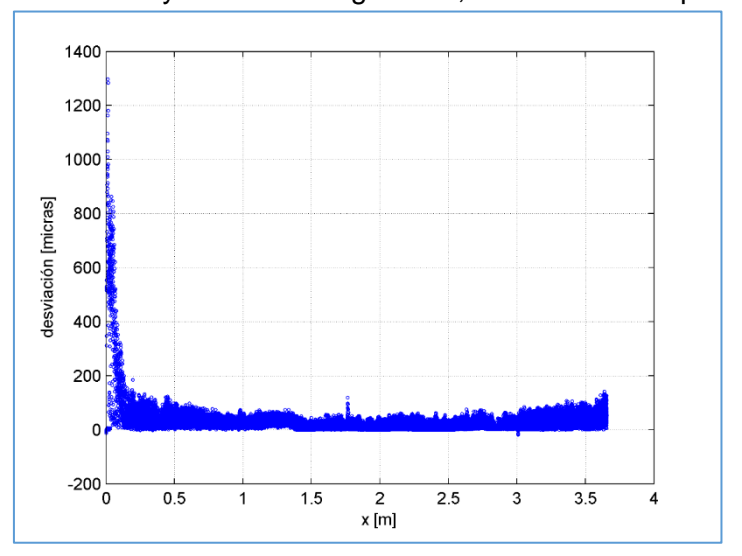


Figure 3 – Departure from the ideal radius. MU1 grid.

Regarding the MU2 grid, the values of $diff(x_i)$ at the first x-sections are very small compared to those of the MU1 grid. The maximum values reduce to 10^{-2} µm approximately. This deviation is very small. The departure from the ideal radius is minimum, no more than 10^{-2} µm. For MU1 mesh, there were values up to 50 µm. A graphical view of the differences between both surface meshes in the tip nose is plotted in Fig. 4.

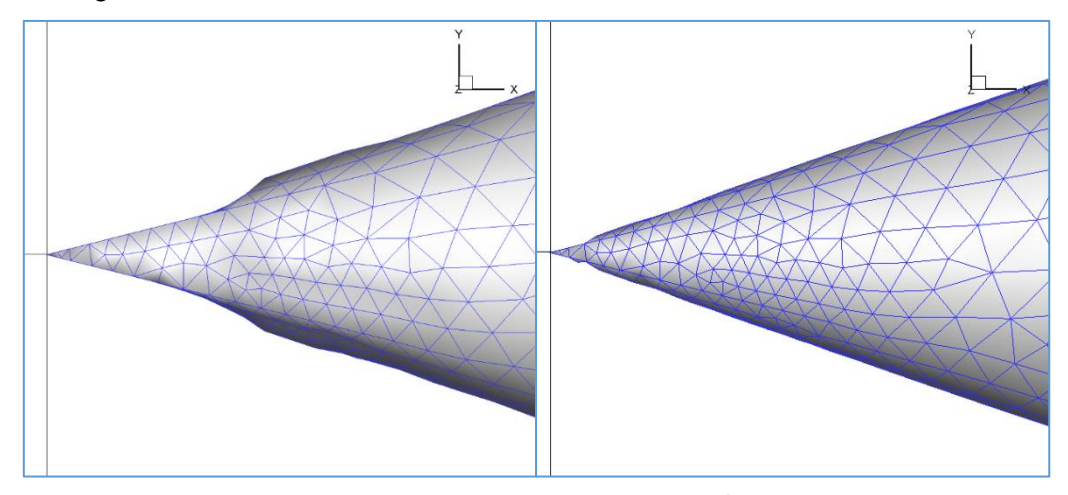


Figure 4 – Detail of the surface mesh at tip nose for roll angle Φ = 0 deg. Left: MU1 grid. Right: MU2 grid.

The procedure used for surface mesh improvement has avoided surface mesh irregularities at the tip nose region. Nevertheless, the unstructured grid at the surface leads to not-even distribution of the cells in azimuth direction. This has an important effect on the calculations, via a roll (orientation) angle dependence of the forces at high angles of attack, larger than the angle of attack for onset of asymmetry. The flow at these conditions is asymmetric, and the uneven distribution of the cells produces important roll angle effects. There is a convective (spatial) instability which adds to the global (temporal) instability due to small flow perturbations at the tip nose.

2.2.2 Grid MU3

This grid was generated with another mesh generator. It is also a hybrid unstructured grid.

The information of the irregularity of the third unstructured mesh, generated with the Centaur[©] grid generator code, is depicted in Fig. 5.

It is interesting to observe how smooth the surface is in the cylindrical part. The departure is less than 1 μ m. But in the ogive region the values of $diff(x_i)$ are larger than those obtained with the MU1 grid, but there is clearly lower roughness, as this curve is more uniform compared to the correspondent of the reference grid MU1 (not shown here). At the tip nose the curve is smoother and the values of $diff(x_i)$ are lower than those of the reference grid.

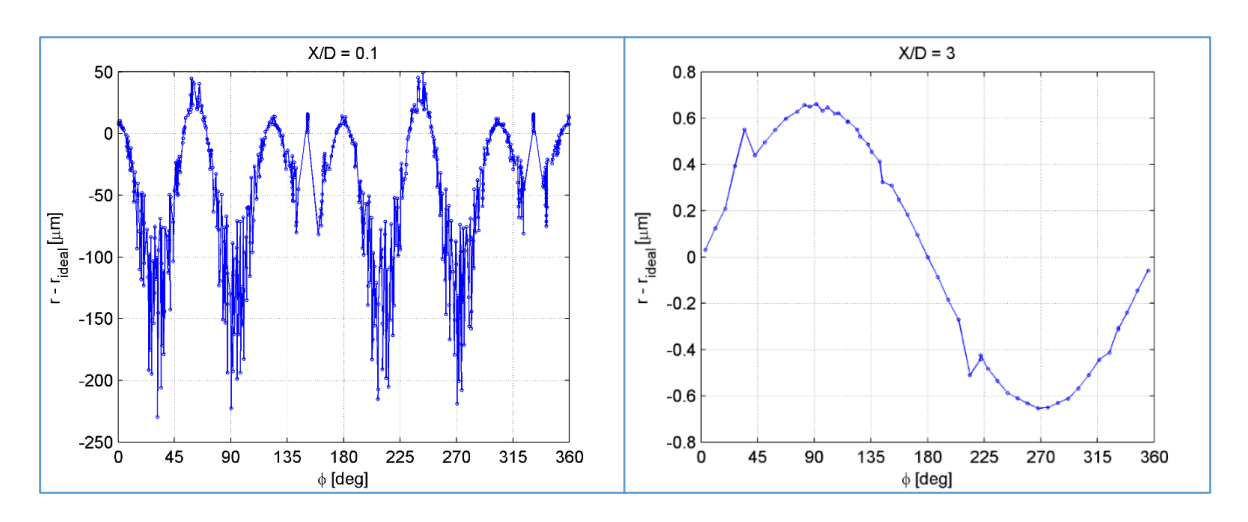


Figure 5 – Departure from the ideal radius. Left: Cross section x/D = 0.1 (tip). Right: Cross section x/D = 3.0 (cylindrical part). MU3 grid.

This information gives us the idea that the grid generated with the CENTAUR® mesh generator, although coarser (see Table 1) is less irregular than the MU1 grid, and has lower level of roughness. This surface mesh resembles a smooth but irregular body at the tip.

3. Grid effect on the forces and moments at several roll angles

The calculations for this M823 bomb configuration were done at transonic flow conditions for different angles of attack, from 0 to 30 deg., and for three roll angles (Φ): 0, 22.5 and 45 deg. It must be reminded that the fins set is form by four fins. Then, a roll angle of Φ = 0 means a cruciform configuration, and for Φ = 45 deg. we have a cross configuration. For Φ = 22.5 deg. it is an intermediate configuration. There is another one, Φ = 67.5 deg., which is the mirror configuration of the former.

There were experimental data for the normal force coefficient, and for the pitching moment coefficient at these three different roll –or azimuth- angles [30-31]. Unfortunately, there was no information on the side force coefficient.

The calculations were done using a Reynolds stress turbulence model (ω -RSM) and they all were steady computations, although transient calculations may be needed for the high angles of attack cases. Internally, transient calculations with the ω -RSM-SAS turbulence model were done in order to

check the solutions with those steady computations solutions. No major differences were found. Anyway, for achieving accurate solutions, these transient calculations with the ω -RSM-SAS turbulence model are mandatory.

The results for the side and normal force coefficients are given in Fig. 6 for the grids MU1 and MU2 at three different roll angles. The pitching moment coefficient is plotted in Fig. 7.

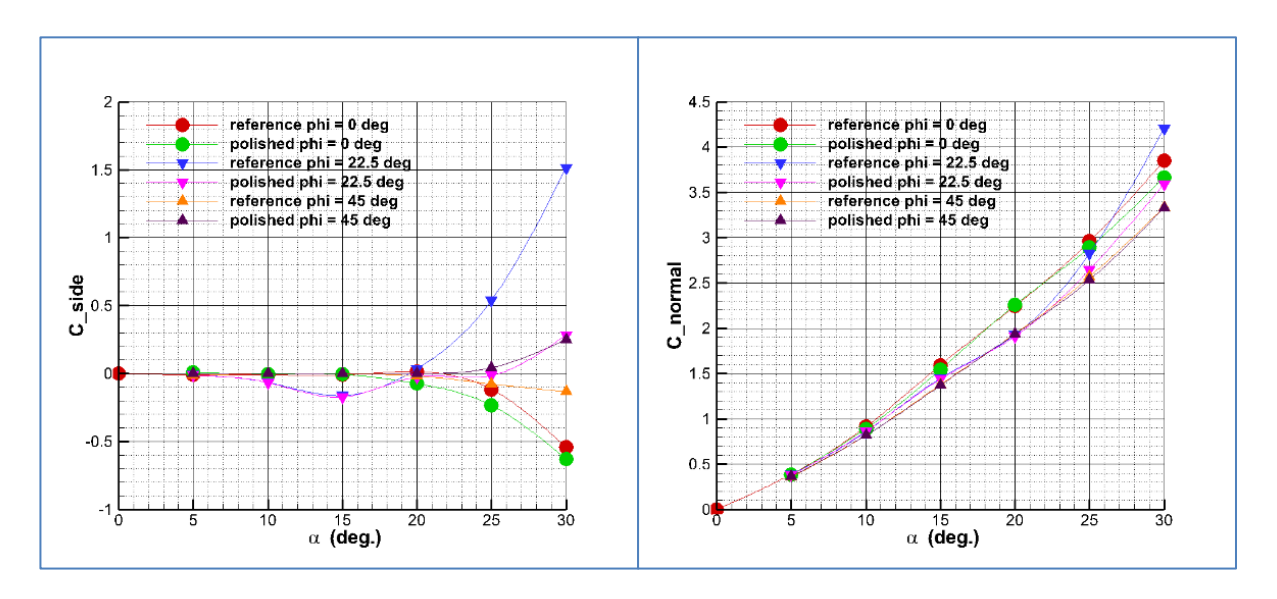


Figure 6 – Side (left) and normal (right) force coefficients versus angle of attack at Ma = 0.85 and Reynolds number Re = $3.4 \cdot 10^6$. MU1 (reference) and MU2 (polished) grids results.

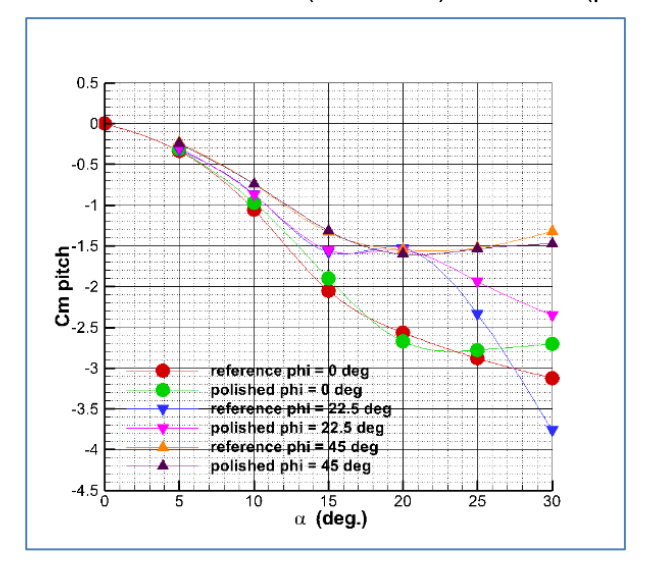


Figure 7 – Pitching moment coefficient versus angle of attack at Ma = 0.85 and Reynolds number Re = $3.4 \cdot 10^6$. MU1 (reference) and MU2 (polished) grids results.

There is a very interesting and unexpected result at the roll angle Φ = 22.5 deg. and for the large angles of attack (α = 25 and 30 deg.). For the cruciform and cross configurations (Φ = 0 and Φ = 45 deg.), the solutions of side and normal force coefficients are very similar for both grids, being MU2 a polished MU1 grid, as it was explained before. For the side force coefficient, at α = 30 deg and Φ = 45 deg. this coefficient is negative when calculating with the reference grid, while it is positive when using the polished (MU2) grid. The absolute values are not equal. One solution may be a mirror of the other provided no fins set is installed. Some coupling effect of the vortices developed at the body with the fins set may exist, and this is different depending on the grid. Anyway, this side force coefficient is small at the larger angle of attack. The angle of attack for onset of asymmetry seems to be close to 25 deg. looking at the side force coefficient curve.

The differences in pitching moment at the larger angle of attack may be related with the small differences in side force, as a different flow pattern exist in the aft region where the fins set is located. However, for the roll angle of Φ = 22.5 deg. the side, normal and pitching moment coefficients differ greatly regarding the other two roll angles. At this roll angle, the angle of attack for onset of asymmetry reduces to 20 deg. and the side force coefficients is too large compared to the other roll angles solutions.

The comparison of the MU1 grid solution with the experimental data is shown in Fig. 8.

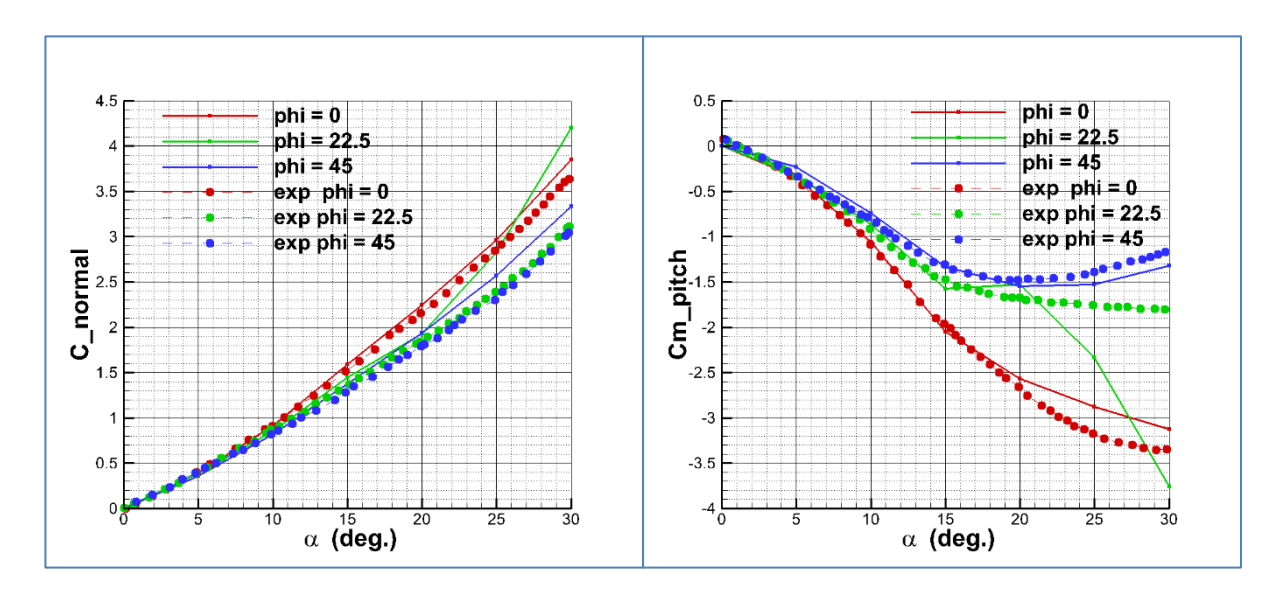


Figure 8 – Normal force (left) and pitching moment (right) coefficients versus angle of attack at Ma = 0.85 and Reynolds number Re = 3.4·10⁶. MU1 grid results and experimental data.

It is clear that the solution for Φ = 22.5 deg. differs from the experimental data at the larger angles of attack —when the side force is too large according to the numerical solution- while for the cruciform and cross configurations the comparison with the experimental data is good. The solutions obtained by MU2 grid are more similar to the experimental data, also at the roll angle Φ = 22.5 deg.

There is another grid -the MU3 grid- generated with other mesh generator. Calculations at the same conditions were done. The normal force and pitching moment coefficients obtained with MU2 (polished MU1) and MU3 (smooth model) grids are compared to the experimental data in Fig. 9.

The MU2 grid normal force coefficient compares well with the experimental data at all angles of attack. The values given by MU3 grid are a little bit larger at the large angles of attack.

Both solutions are very similar at roll angle Φ = 45 deg. (cross configuration) and the normal force coefficient is larger than the experimental one at the large angle of attack range.

The solution at roll angle Φ = 22.5 deg. are again similar for both grids. Anyway, the trend of the normal force coefficient curves is the same for the three roll angles and both grids solutions, and the agreement with the experimental data is fair.

Regarding the pitching moment coefficient the major difference between both numerical solutions is obtained at angle of attack α = 30 deg. and roll angle Φ = 0 deg. (cruciform configuration) due likely to a different interaction of the vortex pair with the fins set. The configuration MU2 has a larger side force. That means that the vortex pair developed at the leeside is more asymmetric and the interaction with the vertical fin is different, contributing also to the pitching moment coefficient. In general, the comparison with the experimental data is also fair.

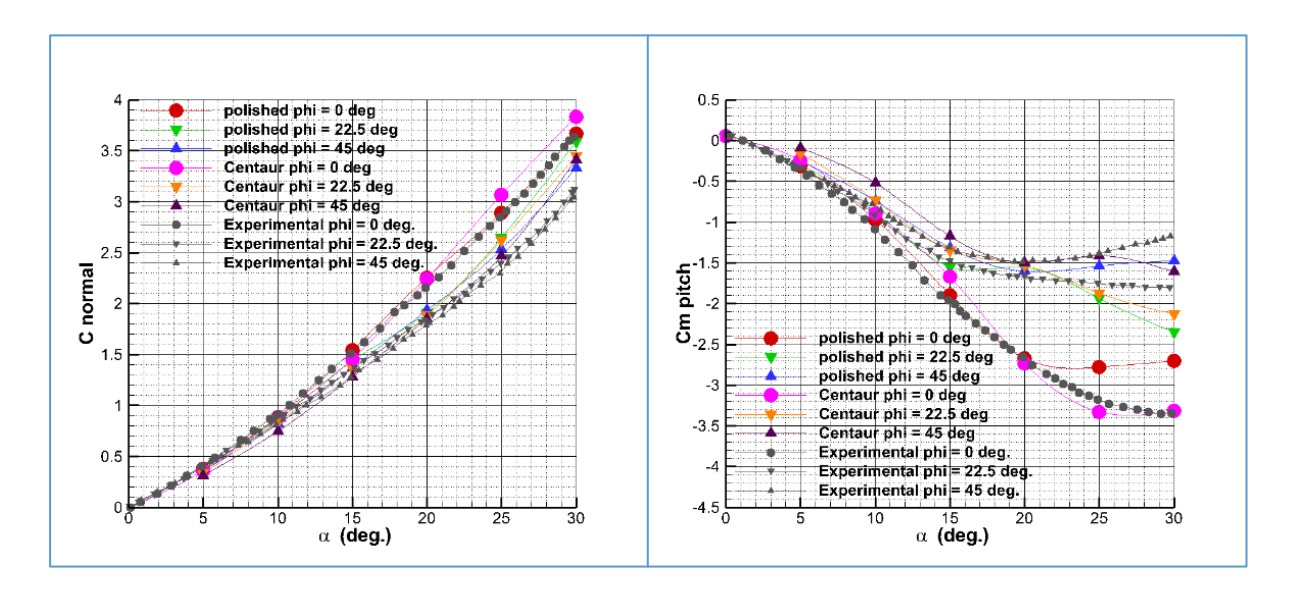


Figure 9 – Normal force (left) and pitching moment (right) coefficients versus angle of attack at Ma = 0.85 and Reynolds number Re = 3.4·10⁶. MU2 (polished) and MU3 (Centaur) grids results and experimental data.

In order to check better the differences between the solutions of both grids MU1 and MU2, total pressure contours and skin friction lines at roll angle Φ = 22.5 deg. are plotted in Fig. 10 for the larger angle of attack, i.e, α = 30 deg. Additionally, vorticity magnitude contours and skin friction lines are plotted in Fig. 11, and finally positive Q-criterion contours and skin friction lines are plotted in Fig. 12.

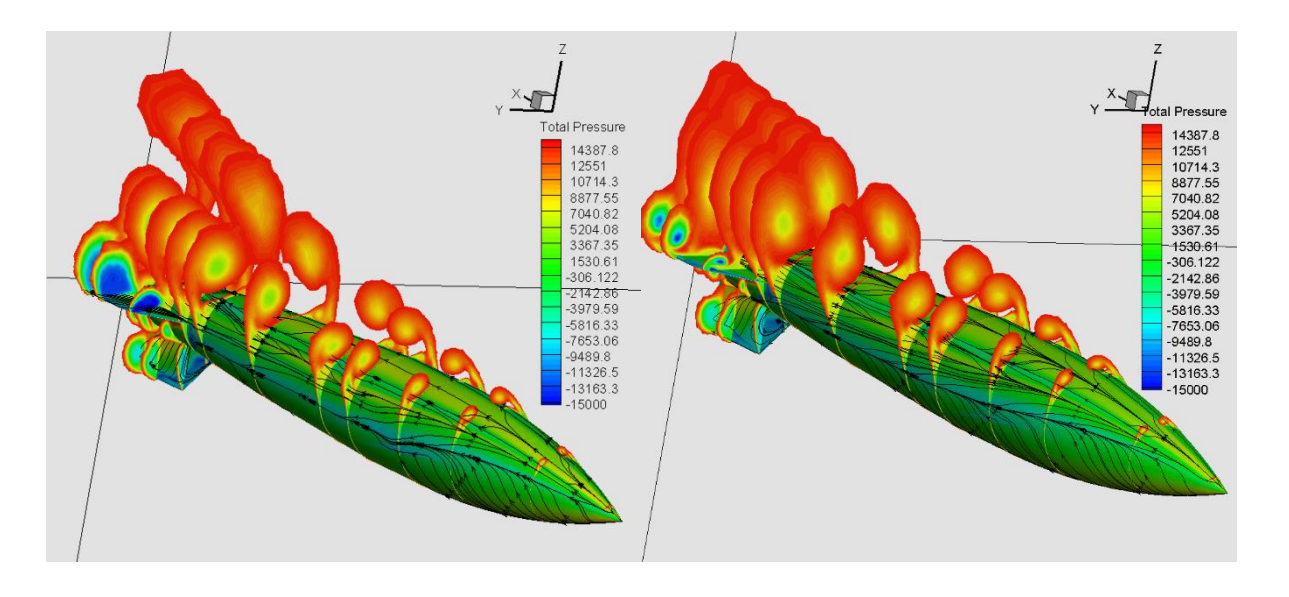


Figure 10 – Total pressure contours and skin friction lines at angle of attack α = 30 deg. and roll angle Φ = 22.5 deg. at Ma = 0.85, Re = 3.4·10⁶. MU1 grid (left) and MU2 grid (right).

It is important to remark, according to references [32-33], that vortices are coherent structures, but not all coherent structures are vortices. Vorticity may be a criterion to identify a coherent structure, but cannot distinguish between swirling motions and shearing motions [32]. Looking at the Fig. 10 and Fig. 11 we can check that the total pressure and vorticity magnitude criterion may be equivalent, as they identify the same coherent structures. As mentioned by V. Holmén in reference [33] vorticity is a method for visualizing vortices, but not for identifying them. Different thresholds in the vorticity magnitude can lead to different geometrical coherent structures.

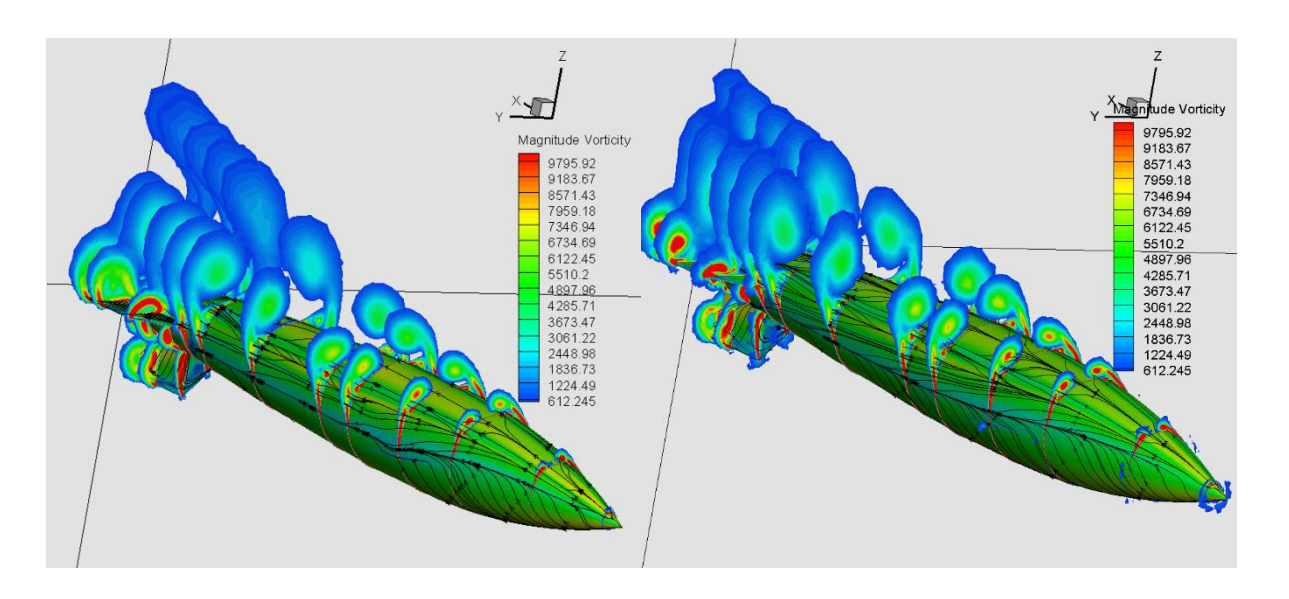


Figure 11 – Vorticity magnitude contours and skin friction lines at angle of attack α = 30 deg. and roll angle Φ = 22.5 deg. at Ma = 0.85, Re = 3.4·10⁶. MU1 grid (left) and MU2 grid (right).

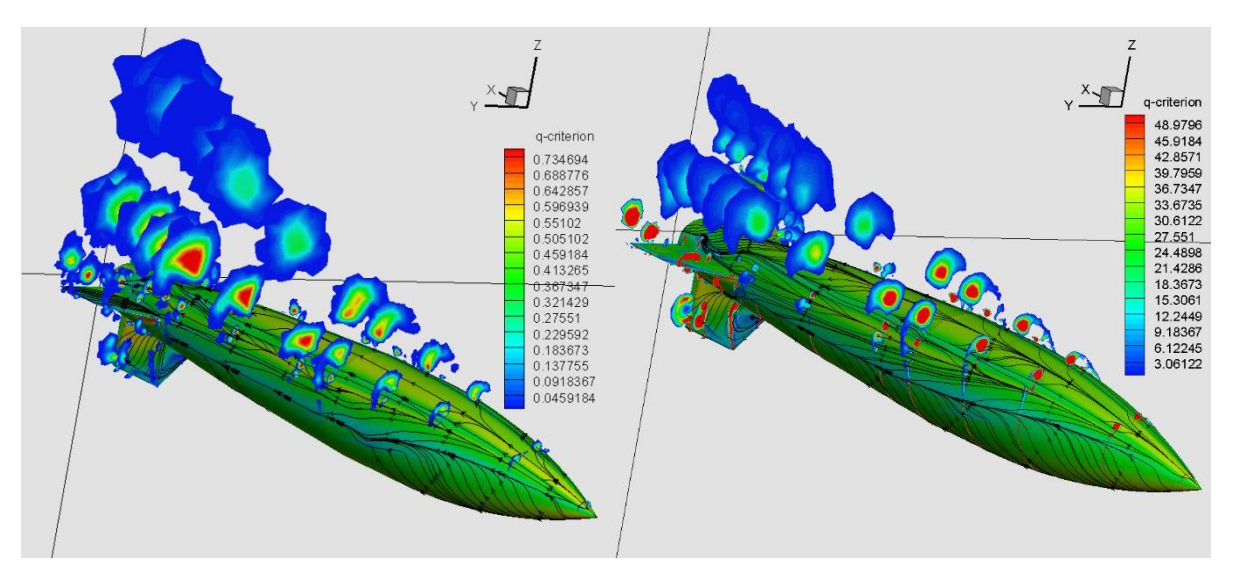


Figure 12 – Positive Q-criterion contours and skin friction lines at angle of attack α = 30 deg. and roll angle Φ = 22.5 deg. at Ma = 0.85, Re = 3.4·10⁶. MU1 grid (left) and MU2 grid (right).

There is a difference when using the Q-criterion or Q-function. Positive Q-function values indicate areas where the rotation overcomes the strain, making possible to identify these surfaces as vortex envelopes [32-33]. Then, the geometric structures of Fig. 12 can be identified as vortex envelopes, while those of Fig. 11 include shear layers.

According to the vortex envelopes of the MU2 grid (right side of Fig. 12) the vortices define a quasi-symmetric flow pattern and are detached at the center of the body. For the MU1 grid solution, the detachment is produced forward. The asymmetric pair of vortices is clearly visible from the tip nose. The contours of Fig. 11 for the MU1 grid configuration, indicate the difference between the shear layers of the port side and starboard side, which contribute to the asymmetric flow pattern and to increase the side force. Better insight is needed regarding the secondary shear layer vortices contribution to the side force. A good investigation on secondary shear layer vortices and the merging with the primary vortices is given in reference [16].

The conclusion is that the geometrical irregularities of the tip have a decisive influence at large angles of attack. As seen in the solutions, the angle of attack for onset of asymmetry is about 25-30 deg. The geometrical irregularities of the tip nose for the MU1 grid are so large that trigger a convective

instability, which produces an asymmetric flow pattern. The MU2 grid has smaller geometrical irregularities, particularly in the tip nose. This has been sufficient to reduce significantly the flow asymmetry produced by the pair of vortices of the leeside of the body. Its solution fits well with the solution provided by MU3 grid, which has low geometric irregularities.

The solutions of MU2 and MU3 grids compare better with the experimental data. This indicates that the tip nose resolution is very important for the numerical calculations, and that of MU1 grid is not so adequate. It is needed a better resolution in the tip nose to have confidence in achieving solutions which will reproduce with fair agreement the aerodynamic features detected in the wind tunnel tests.

4. Rolling motion

Rolling is the motion where a missile flies at a constant pitch angle, with respect to the freestream velocity vector while undergoing a constant angular rotation about its x-axis (nose-to-tail direction).

An effect of this motion is the appearance of a Magnus contribution to the side and normal force and yawing moment, and a roll damping moment. Classical studies of the rotation of a body of revolution in crossflow led to the definition of the Magnus effect, which consists of the appearance of forces parallel and normal to the incoming flow when the body is rotating [25]. Nielsen, when studying the missile's motion, defines the Magnus forces and moments as those developing as a result of rolling at an angle of attack [26]. For missiles, the Magnus effect of the body is usually small compared to that of the fins. The classical approach considers the Magnus side force linear with the reduced roll rate and the angle of attack. This is a good approach for low angles of attack [26]. Using the Maple—Synge analysis, some researchers showed that there are in-plane and out-of-plane Magnus terms [27]. They developed a model of the non-linear forces in rolling motion. Liaño *et al.* used a strong non-linear model for the pitching moment to study the lateral motion of missiles [28-29]. Therefore, for rolling motion at high angles of attack studies, a question that arises is the appearance of non-linear effects similar to those described in these references.

Regarding the calculations of rolling motion for the M823 bomb configuration, the range of angle of attack is [0, 30] deg. At the larger angles of attack the flow is not symmetric: there is a side force, which in most cases is small compared to the normal force. There is a configuration for which the side force is large due to an important flow asymmetry at the body. This is an effect of the geometric irregularities. This has been explained above. As these irregularities have an important effect in steady motion calculations (without rolling), they may also have an influence in the Magnus effect, in terms on non-linear effects.

4.1 Theoretical background

Nielsen defines Magnus forces and moments as those developing as a result of rolling at an angle of attack [26]. The term $C_{ip\alpha} \left(\frac{p \cdot D}{2V_{\infty}} \right) \cdot \alpha$ or $C_{ip\alpha} \left(\frac{p \cdot D}{2V_{\infty}} \right) \cdot \sin \alpha$ is normally defined as the Magnus effect term.

The first expression is accurate only for small angles of attack. The second one is more general. These terms have been numerically estimated in several CFD studies, such as those carried out by Bhagwandin for a missile-type configuration [34]. After a transient, the motion is periodic, and the side force coefficient C_{γ} is computed as the averaged value in one rotation. This is conducted at several roll rates. The slope at each angle of attack is the Magnus side force spin derivative coefficient $C_{\gamma p}$ which permits calculating the Magnus side force derivative coefficient $C_{\gamma p}$ when plotting versus the angle of attack (or versus $\sin \alpha$).

In general, for a missile-type configuration formed by an axisymmetric body and a set of two, three or four fins, based on symmetry considerations, the Maple-Synge analysis can be used to model the force and moment coefficients and also their stability derivatives [26]. However, this is not valid for high angles of attack due to flow separation. Moreover, at high angles of attack, the flow is asymmetric for an axisymmetric configuration, due to the non-symmetric flow pattern from the tip on. Therefore, this theory is not appropriate to determine accurately the forces and moments coefficients, and particularly their derivatives, which are important for stability and control characteristics.

In reference [27], a high-order model for a missile configuration (body and a set of fins) has been

developed; the Magnus side force is characterized as:

$$C_{yMagnus} = \left(\frac{p \cdot D}{V_{\infty}}\right) \begin{bmatrix} 2C_{N\alpha 0} \cdot W^{011} \cdot \alpha_{total} + \frac{9}{2}C_{N\alpha 2} \cdot W^{211} \cdot \alpha_{total}^{3} + \left(\frac{3}{4}C_{N\alpha 2} \cdot W^{031} + \frac{25}{4}C_{N\alpha 4} \cdot W^{411}\right) \cdot \alpha_{total}^{5} \\ + \frac{75}{16}C_{N\alpha 4} \cdot W^{231} \cdot \alpha_{total}^{7} + \frac{15}{64}C_{N\alpha 4} \cdot W^{051} \cdot \alpha_{total}^{9} \end{bmatrix}$$
(2)

The terms W are weighting factors, and the coefficients $C_{\scriptscriptstyle N\alpha}$ are fin-alone coefficients. Details are given in the reference [27]. In this model, there is not only a term for linearity with the reduced roll rate and angle of attack, but also higher order terms for the angle of attack. Liaño et~al. studied the influence on the free flight motion of a missile of a nine-order roll-dependent model of the pitching moment slope coefficient $(C_{\scriptscriptstyle m\alpha})$ [28-29]. Corresponding complex models can be derived for other coefficients, including the Magnus terms. These models described in references [27-29] show that there may be important terms not taken into account in a simple approach.

High-level CFD codes, which solve the unsteady Reynolds averaged Navier–Stokes (URANS) equations with complex turbulence models, have become reliable tools for computing the flow in regions where nonlinear effects are very important. Using CFD calculations, the forces and moments can be estimated, and their stability derivatives may be calculated using a finite difference approach or other methods. Additionally, nonlinear effects can be studied by analyzing the solutions. The numerical calculations presented herein have been performed using an axisymmetric configuration with fins –the bomb M823- at low to moderate angles of attack.

4.2 Rolling motion: MU1 and MU2 grids

For determining some stability derivatives and Magnus effect, a rolling motion is simulated at a constant spin rate about the body x-axis. The grids MU1 and MU2 are used. MU1 grid, which is the grid with more geometrical irregularities in the tip nose, was firstly used for the computations.

Time accurate computations are needed, and the sliding mesh technique is used. The grid is divided in two subdomains (see Fig. 2). The first subdomain (inner cylinder) rotates with the body, and the second one is fixed. In the interface between the two subdomains, special interpolation is used for the fluxes conservation. Care must be taken to avoid accumulative errors. It is convenient to make the calculations in one step, instead of making successive steps due to errors of interpolation. As the calculations are intrinsically transient computations, the ω -RSM-SAS turbulence model has been used [19-24]. This turbulence model is less dissipative.

The roll damping moment and Magnus derivatives may be proportional to the spin rate p.

It is common practice to non-dimensionalize the spin rate as $\Omega = p' = \left(\frac{p \cdot D}{2V_{\infty}}\right)$. This is the non-dimensional roll rate. With p (rad / s) as the spin velocity (angular velocity), the frequency is

 $f = \frac{p}{2\pi} = \left(\frac{V_{\infty} \cdot \Omega}{\pi \cdot D}\right)$ (1/s). Nielsen, when studying the missile's motion, defines the Magnus forces and

moments as those developing as a result of rolling at an angle of attack [26].

The side and normal Magnus forces have the following expressions:

$$F_{Magnus\ side} = \frac{1}{2} \rho_{\infty} \cdot V_{\infty}^{2} \cdot S \cdot \left(\frac{p \cdot D}{2V_{\infty}}\right) \cdot C_{Yp\alpha} \cdot \sin \alpha$$

$$F_{Magnus\ normal} = \frac{1}{2} \rho_{\infty} \cdot V_{\infty}^{2} \cdot S \cdot \left(\frac{p \cdot D}{2V_{\infty}}\right) \cdot C_{Zp\alpha} \cdot \sin \alpha$$
(3)

being $S = \frac{\pi \cdot D^2}{4}$ the reference area.

For small angles of attack $\sin \alpha \approx \alpha$. There is also a Magnus yaw moment, defined similarly as:

$$M_{Magnus\ yaw} = \frac{1}{2} \rho_{\infty} \cdot V_{\infty}^{2} \cdot S \cdot D\left(\frac{p \cdot D}{2V_{\infty}}\right) \cdot C_{np\alpha} \cdot \sin \alpha \tag{4}$$

In a rolling motion, it appears a rolling damping moment defined as:

$$M_{roll} = \frac{1}{2} \rho_{\infty} \cdot V_{\infty}^2 \cdot S \cdot D \left(\frac{p \cdot D}{2V_{\infty}} \right) \cdot C_{lp}$$
 (5)

For CFD calculations, a prescribed roll technique is used. Several spin rates are chosen and the forces and moments at these cases are computed. By finite differences approach the derivatives C_{yp} , C_{zp} , C_{pp} and C_{pp} can be estimated and then, the Magnus derivatives.

A derivative may be calculated using finite difference approach based on the average force or moment for two spin rates as: $C_{ip} = \left(\frac{C_{ip2} - C_{ip1}}{p_2 - p_1}\right)$ [35]. For linear approach, the derivative may be constant at a

wide range of spin rates. Then, only two roll rates may be enough for the computations. For non-linear approaches, the forces and moments must be calculated at a large number of spin rates. As it is not practical –in terms of computational costs- to perform many computations, only three spin rates were chosen for the initial calculations. These spin rates are: $p = 2\pi, 10\pi, 20\pi (rad/s)$, i.e., f = 1, 5, 10 (Hz)

The period of rotation is $T = \frac{1}{f} = N \cdot \Delta t$ being Δt the time step and N the number of numerical iterations per rotation. For the time step chosen, we focus on the largest spin rate, $p = 20\pi \, rad/s$, i.e.,

10 Hz. That means 10 cycles/s. This is equivalent to 3600 deg/s. A time step $\Delta t = \frac{1}{3600} = 2.77 \cdot 10^{-4} \text{ s}$

is considered sufficient. In this time step, the body rotates 1 deg. For the lowest spin rate of $p = 2\pi$ rad/s, the body rotates 0.1 deg. in this time step. For the transient calculations, dual time stepping technique was used and the turbulence model was the ω -RSM-SAS model [19-24]. This turbulence model permits to achieve LES-like solutions provided the grid size is small and the time steps adequate to obtain Courant-Friedrichs-Levy (CFL) numbers close to 1. The number of iterations depend on the case. First calculations using MU1 grid have been done such that N is 1800 for the lowest spin rate and 7200 for the larger one. The value N = 1800 may not be sufficient as only half cycle is completed after this time, $T = N \cdot \Delta t = 0.5$ s. For the largest spin velocity the time usually chosen is $T = N \cdot \Delta t = 2$ s as the number of time steps was N = 7200. Depending on the angle of attack and spin rate, either 1800, 3600 or 7200 number of time steps have been chosen.

Parameter	Case 1	Case 2	Case 3
p (rad/s)	2π	10π	20π
f (Hz)	1	5	10
Ω	0.00584	0.02922	0.05844
Δt (s)	0.000277	0.000277	0.000277
N iterations per rotation	3600	720	360
N iterations (MU1 grid)	1800/3600	3600	3600/7200
N. iterations (MU2 grid)	7200	1440	720
Inner time-steps	20	20	20

Table 2 – Rolling motion: Numerical attributes. MU1 and MU2 grids

Regarding the MU2 grid, two complete cycles at each spin velocity were calculated. This is detailed in Table 2.

Calculations at angles of attack {5, 10, 25, 30} deg. were done at the three spin rates for MU1 grid. For MU2 grid, calculations at angles of attack {10, 25, 30} deg. were done. Then, using the results of the last rotations, the total coefficients were computed as averages over the last half rotation or the last rotation. These coefficients may be plotted as a function of the spin rate, and therefore, with finite differences or other interpolation approach, the derivatives and Magnus forces derivatives can be estimated.

4.3 Rolling motion: forces and moments

The averaged force and moment coefficients at three spin rates are calculated for several angles of attack: {5, 10, 25, 30} deg.

The side and normal force coefficient versus angle of attack at the spin rates used for the calculations are plotted in Fig. 13 whilst the roll and yawing moment coefficients are plotted in Fig. 14. For the steady state, i.e., p = 0 Hz, both solutions of cruciform and cross configurations are plotted.

It is important to remark that at the larger angle of attack of α = 30 deg. the side force at p = 0 Hz is negative for the cruciform configuration, with an absolute value of 0.5415 for MU1 grid. The experiments for different bodies at high angle of attack, as well as numerical investigations [1, 5, 6] indicate that there is a bi-stable possible solution. Then, for other initial solutions it would be possible to have a positive side force. Computations made by the author at positive spin rates for an ogive-cylinder configuration at high angle of attack led to positive side forces, whilst computations at negative roll rates led to negative side forces, indicating an effect of the spin rate in fixing the sign of the side force [36]. The body and vertical fin are the main contributors to the side force. The yawing moment curve is very similar to the side force curve, as they are related. The rolling moment values at the larger angles of attack are due to the side force contribution of the vertical fin. Rolling at negative spin rates are then recommended in order to have a deeper insight at large angles of attack.

It is worth noting that at angle of attack α = 25 deg. the rolling moment is positive for the lower spin rates and MU1 grid configuration. There is no damping. There is a complex interaction of the vortex pair shed at the leeside of the body with the fins.

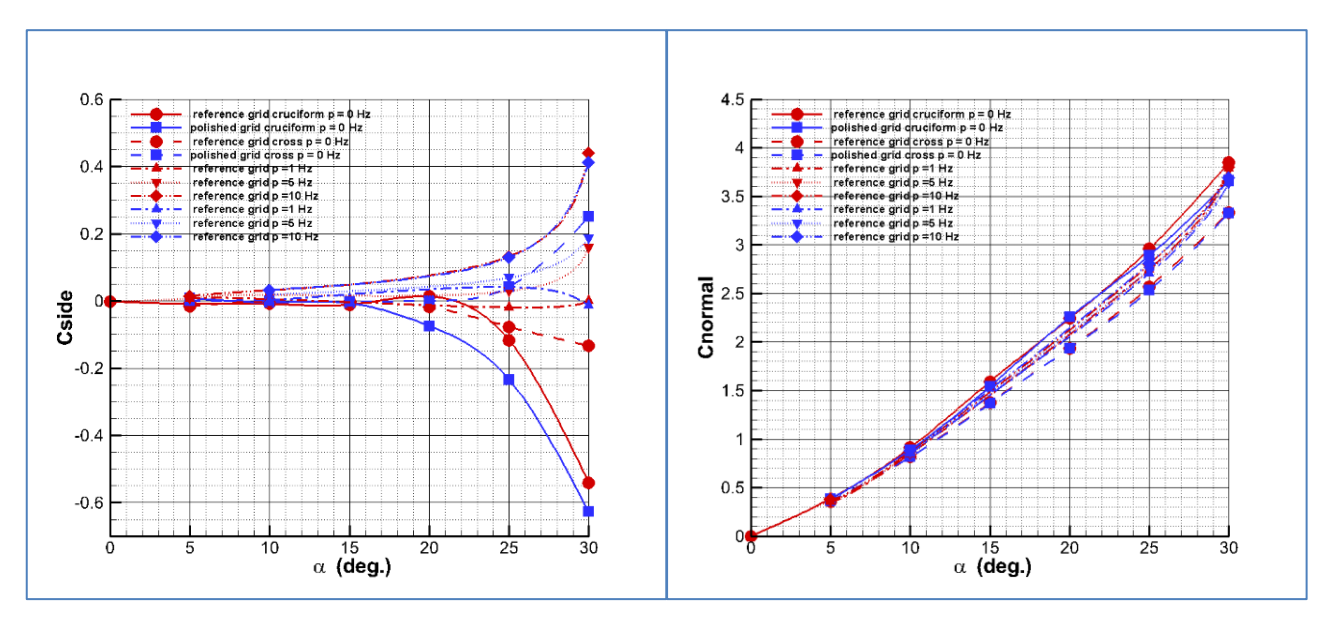


Figure 13 – Side and normal force coefficients versus angle of attack at several spin rates at Ma = 0.85 and Reynolds number Re = 3.4·10⁶. MU1 and MU2 grids.

The range of angle of attack is $\{0, 30\}$ deg. As the value of $\sin \alpha$ is 0.4226 at angle of attack α = 25 deg., i.e., 0.4363 (rad), and this value is 0.5 at angle of attack 30 deg., i.e., 0.5235 (rad), the use of $\sin \alpha \sim \alpha$ is accurate for this range. Then, a plot of the force and moment coefficients versus $\Omega \cdot \alpha \sim \Omega \cdot \sin \alpha$ (rad) has been used for the determination of Magnus force derivative coefficient $C_{\gamma p \alpha}$ and Magnus moment derivative $C_{Np \alpha}$. The roll damping moment C_{lp} can also be determined.

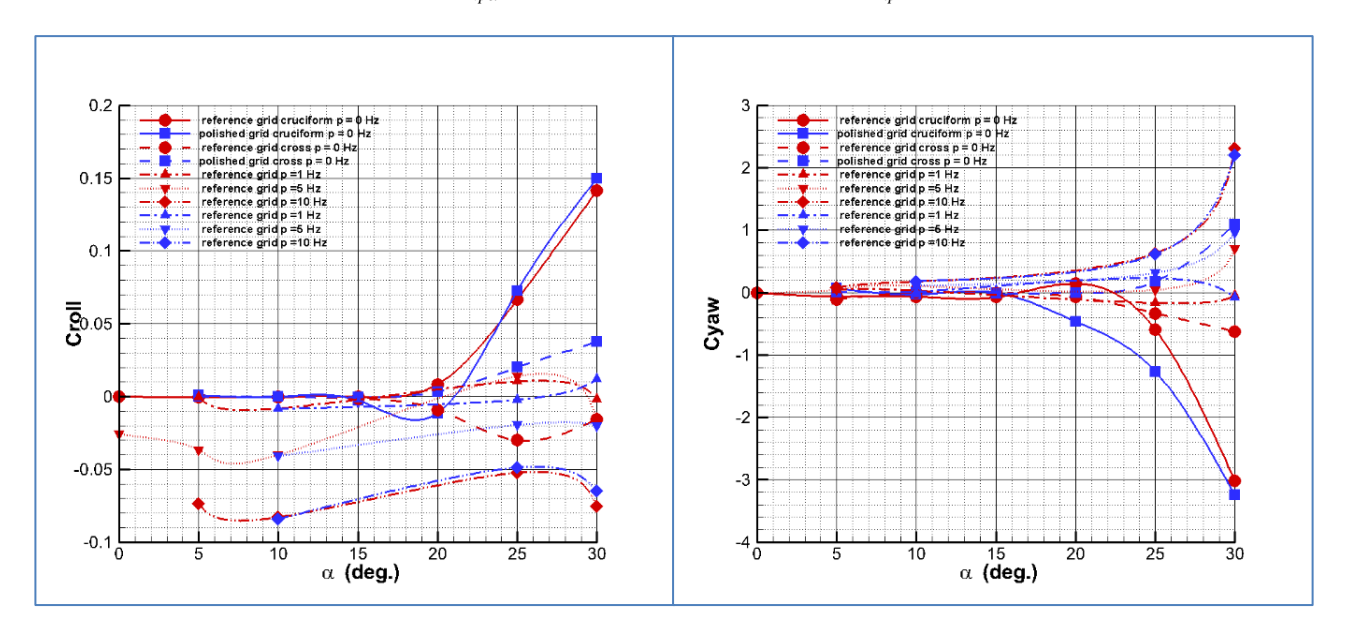


Figure 14 – Roll and yawing moment coefficients versus angle of attack at several spin rates at Ma = 0.85 and Reynolds number Re = 3.4·10⁶. MU1 and MU2 grids.

The first conclusion observed in the following figures (Fig. 15 and Fig. 16) is that the Magnus side force is not linear with the roll rate at the larger angles of attack, particularly for the angle of attack α = 25 deg. and for MU1 configuration. The effect in normal force is small.

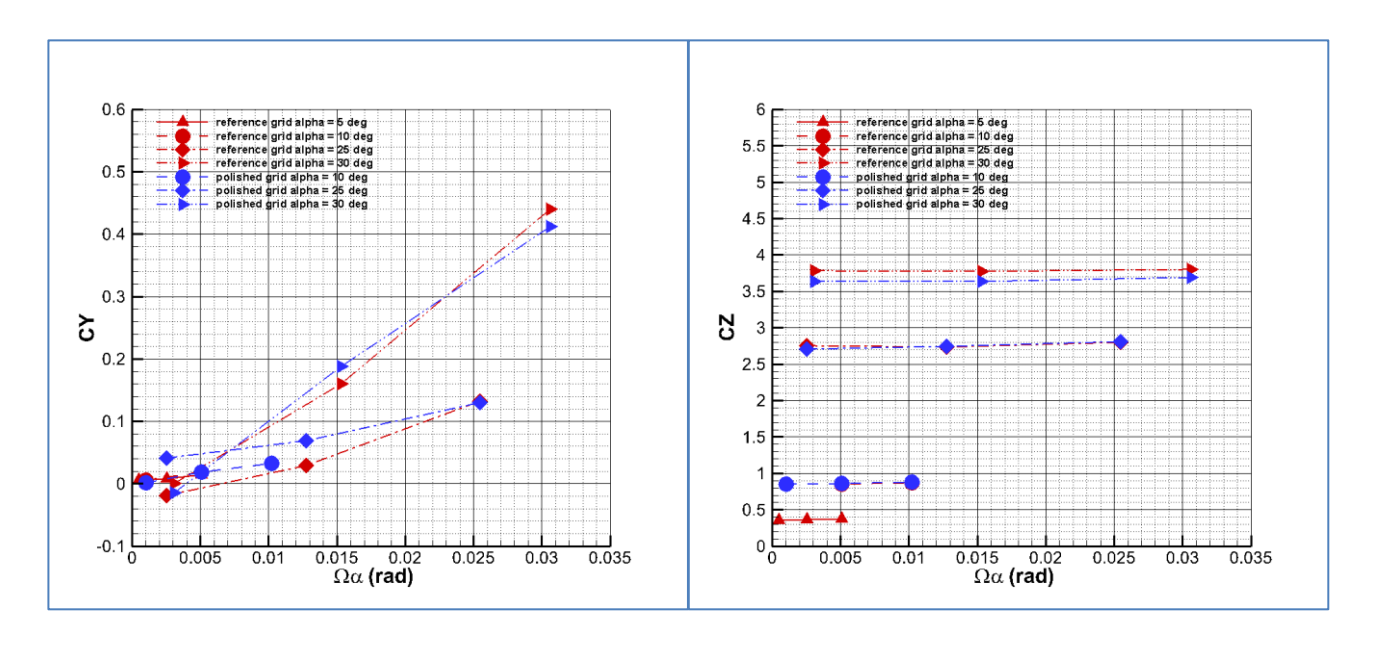


Figure 15 – Side and normal force coefficients versus the non-dimensional roll rate and angle of attack at several angles of attack at Ma = 0.85 and Reynolds number Re = 3.4·10⁶. MU1 and MU2 grids.

Similar conclusion is obtained for the Magnus yawing moment. Regarding the rolling moment, the Magnus derivative is not constant for low spin rates and again at angle of attack α = 25 deg. for the MU1 grid configuration. An asymmetric vortex pair formed at the tip nose develops downwards and the interaction with the fins is important to produce a rolling moment different to that produced when calculating the MU2 configuration, which resembles a similar configuration with reduced roughness and tip geometrical irregularities.

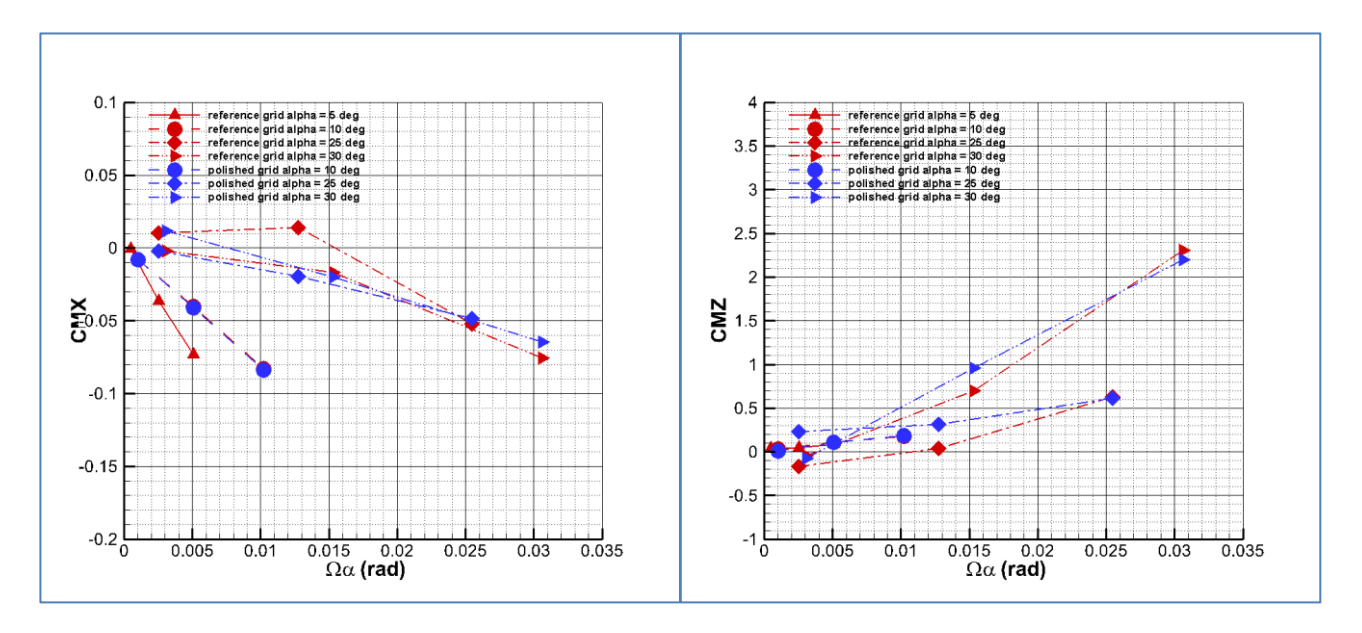


Figure 16 – Rolling and yawing moment coefficients versus the non-dimensional roll rate and angle of attack at several angles of attack at Ma = 0.85 and Reynolds number Re = 3.4·10⁶. MU1 and MU2 grids.

The rolling moment coefficients versus roll rate shown in Fig. 17 indicate that the roll damping moment coefficient C_{lp} is non-linear at large angles of attack, basically when using the MU1 configuration.

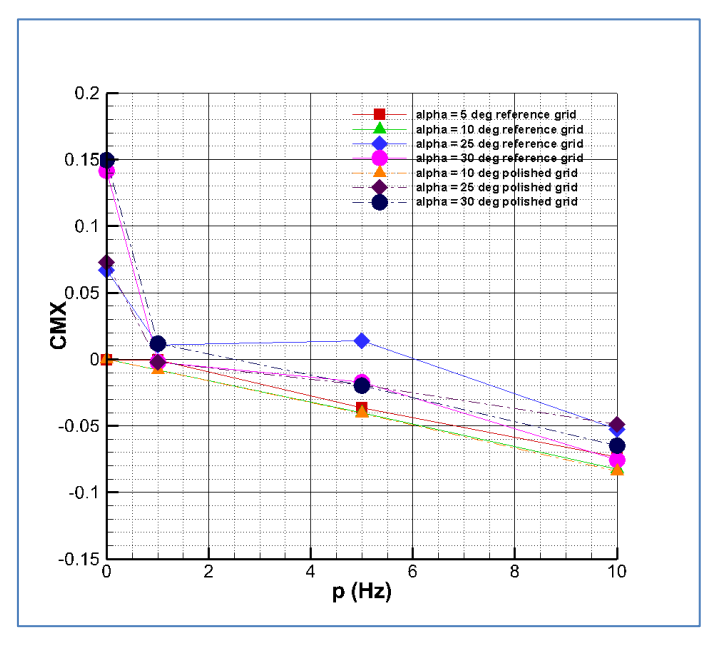


Figure 17 – Rolling moment coefficient versus the roll rate at several angles of attack at Ma = 0.85 and Reynolds number Re = 3.4·10⁶. MU1 and MU2 grids.

A question that arises regarding these calculations is the possible spurious nonlinear effects due to the tip nose geometrical irregularities of the surface mesh of MU1 grid. The results of MU2 grid, which resembles a polished and more symmetrical configuration of the body, indicate a more linear behavior, especially at large angles of attack. Therefore, it can be checked that there is a quantitative large effect of grid irregularities in computing the stability derivatives and Magnus derivatives for low spin rates.

5. Accuracy of the transient calculations

The turbulence model ω -RSM-SAS [19-24] has been used for the transient calculations. Some comments on the accuracy of the model follows. The advantage of Scale Adaptive Simulation (SAS) is the ability of the model to "adjust to the mesh and time step resolution provided, resulting in a continuous variation of the simulation from LES to steady-state RANS" in words of Menter *et al.* [21]. In this reference, there is a comparison of solutions obtained with the same mesh and different time steps, from one typical LES time step (CFL < 1) to other 40 times larger. F. R. Menter remarks that "if the grid is not of LES resolution, SAS will still produce sensible results, and under coarse meshes and or large time steps will fall back to the RANS solution" [21]. The use of small time steps that lead to solutions with Courant numbers close to 1, will provide LES-like solutions also in "coarse" grids. The grids MU1 and MU2 are grids of approximately 13 million cells (see Table 1). Then, the time step should be small enough in order to resolve scales up to their grid limit.

It is worth noting that the calculations for zero spin rates were steady state calculations, using a Reynolds Stress turbulence model (RSM). SAS is only used for transient calculations. But, at the high angles of attack -and for the MU1 grid- transient calculations were carried out using the ω -RSM-SAS turbulence model, in order to verify that the solution was steady.

According to Champigny, "a time-space equivalence between the von Karmàn unsteady asymmetric vortex wake in 2-D flow and the steady asymmetric vortex pattern in 3-D flow is often used to describe the vortex shedding process on bodies at high angle of attack [3]. The period of the von Karmàn wake

in the crossflow plane is: $T = \frac{1}{f} = \frac{D}{St \cdot U_{\infty} \cdot \sin \alpha}$. The typical Strouhal number is 0.2 for circular

cylinders. For an ogive-cylinder configuration at low speed, tested and calculated under a *GARTEUR* Group (AG-42) the experimental Strouhal was St=0.16 [18], [37]. Our computations with ω -RSM-SAS turbulence model led to a Strouhal number of St=0.15. Assuming St=0.15 also for this configuration, the period for the larger angle of attack condition ($\alpha=30$ deg.) should be:

$$T = \frac{1}{f} = \frac{D}{St \cdot U_{\infty} \cdot \sin \alpha} = 0.0187 \ s$$
. However, there is also a convective time $T_c = \frac{L}{U_{\infty} \cdot \cos \alpha}$ related

to the characteristic length of the body. At angle of attack α = 0 deg. this time is minimum, and the characteristic length is the total length of the body of the M823 Bomb. Then, $T_c = \frac{L}{U_{\infty} \cdot \cos \alpha} = 0.0050 \, s$

This time scale is smaller than the other one. This period can be used for the time steps determination. Typical time steps of $\Delta t = \frac{1}{30}T$ are used in certain test cases in order to achieve Courant numbers

about unity [23]. For the transient cases at zero spin rate, we used time steps of $\Delta t = 0.0001 \approx \frac{1}{50} T_c$.

The transient solutions showed that the flow was stationary and the normal and side force coefficients differ a little from the steady state solutions at angle of attack α = 30 deg. However, the Courant number was not about unity at the boundary layer region, as can be checked in Fig. 18 (left image). The grid is coarse. More accurate solutions could be obtained reducing the cell size -particularly in the boundary layer region- and/or reducing the time step.

For rolling motion, a time step of $\Delta t = 0.000277 \ s = \frac{1}{3600} \ s$ was used. This is considered accurate to

take into account the effects of rolling, but this time step is larger (almost 3 times larger) than that used in the time-accurate calculations for zero spin. CFL contours at plane y = 0 are plotted in Fig. 18

(right side) for a test case of rolling motion at α = 25 deg. with a roll rate of p = 1 Hz, i.e., 2π rad/s. It can be checked that in the region close to the body where the vortex wake develops, and in the region close to the fins, the Courant numbers lie between [10-30] indicating that a reduction of the time step and a refinement of the mesh near the body and close to the leading edge fins, are advisable in order to capture more accurately the turbulent scales and wake evolution.

We can conclude that, with this time step, the vortex wake may not be accurately computed (LES-like solution), and this has an effect on the vortex and fins interaction, which is important for rolling moment calculations. Reference [38] shows a good survey of the influence of modelling on rolling moment computations. This can be resumed in a computing time of at least one order of magnitude larger than the actual computing times. Unfortunately, the computational resources are very limited for us. Therefore, an optimization of the grids without a large increment of the grid size will be explored. Time steps of the same order than the actual values will be used, except in critical cases, which will help to assess the solutions.

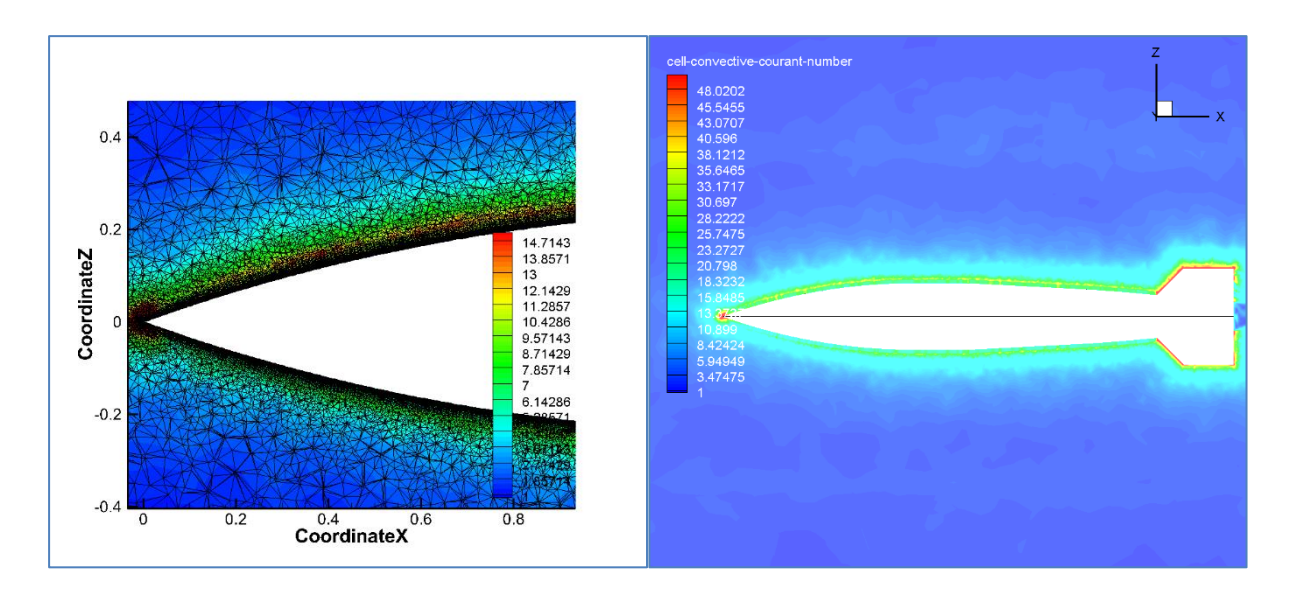


Figure 18 – CFL contours at plane y = 0. Left: angle of attack $\alpha = 30$ deg., roll rate p = 0 and roll angle $\Phi = 22.5$ deg., MU1 grid. Right: angle of attack $\alpha = 25$ deg. at roll rate p = 1 Hz, MU2 grid. Time accurate calculations (ω -RSM-SAS turbulence model).

6. Conclusions

Steady flow computations of a bomb -named M823- have been carried out at a baseline condition in order to compare their results with experimental data, and to analyze the effect of geometrical irregularities on the flow field. To do that, three grids have been used, such that one of the grids has significant geometrical imperfections. The other two grids resemble polished test models, as the size of the geometrical irregularities is small.

At large angles of attack, there is an important roll or orientation angle effect in terms of asymmetric flow, which leads to large side forces for the body of large geometrical irregularities. These irregularities are measured as the departure from the ideal axisymmetric geometry defined.

The numerical solutions of the smooth grids are accurate compared to the experimental data, while the numerical solutions of the rough grid differ from the experimental data at one roll angle, indicating a strong roll angle dependence of the forces and moments.

Prescribed-roll calculations have been done at three roll rates at the different angles of attack in order to analyze the Magnus effect and the roll damping moment coefficient. These results indicate clearly a non-linear dependence of the Magnus force and moment derivatives with the roll rate at large angles of attack. A similar conclusion is obtained for the roll damping moment coefficient.

7. Copyright Statement

The authors confirm that they, and/or their company or organization, hold copyright on all of the original material included in this paper. The authors also confirm that they have obtained permission, from the copyright holder of any third party material included in this paper, to publish it as part of their paper. The authors confirm that they give permission, or have obtained permission from the copyright holder of this paper, for the publication and distribution of this paper as part of the ICAS proceedings or as individual off-prints from the proceedings.

8. Contact Author Email Address

José Jiménez Varona (Flight Physics Department, Theoretical Aerodynamics Lab): jimenezj@inta.es

References

- [1] Champigny, P. High angle of attack aerodynamics *AGARD R-804 Special Course on Missile Aerodynamics*; Specialized Printing Services Limited: Loughton, UK, pp. 5-1 5-19, 1994.
- [2] Champigny, P. Side forces at high angles of attack. Why, when, how? *La Recherche Aerospatiale*, nº 4, 269-282, 1994.
- [3] Champigny, P. Reynolds number effect on the aerodynamic characteristics of an ogive-cylinder at high angles of attack. *AIAA 2nd Applied Aerodynamics Conference*, Seattle, WA, USA, 1984. https://doi.org/10.2514/6.1984-2176.
- [4] Ericsson, L.E. and Reding, J.P. Vortex induced asymmetric loads in 2-D and 3-D flows. *AIAA 18th Aerospace Sciences Meeting*, Pasadena, California, USA, 1980. https://doi.org/10.2514/6.1980-181.
- [5] Bridges, David H. The asymmetric vortex wake problem-Asking the right question. 36th AIAA Fluid Dynamics Conference and Exhibit, San Francisco, CA, USA, 2006. https://doi.org/10.2514/6.2006-3553.
- [6] Hunt, B.L. Asymmetric vortex forces and wakes on slender bodies. *AIAA 9th Atmospheric Flight Mechanics Conference*, San Diego, CA, USA, 1982. https://doi.org/10.2514/6.1982-1336.
- [7] Ramberg, S.E. The effects of yaw and finite length upon the vortex wakes of stationary and vibrating circular cylinders. *Journal of Fluid Mechanics* (1983), Vol. 128, pp. 81-107, 1983. https://doi.org/10.1017/S0022112083000397.
- [8] Degani, D. and Tobak, M. Numerical experimental and theoretical study of convective instability of flows over pointed bodies at incidence. 29th Aerospace Sciences Meeting, Reno, Nevada, USA, 1991. https://doi.org/10.2514/6.1991-291.
- [9] Zilliac, G., Degani, D. and Tobak, M. Asymmetric vortices on a slender body of revolution. *AIAA Journal*, Vol 29, № 5, 1991. https://doi.org/10.2514/3.59934.1-2.
- [10] Degani, D. Development of nonstationary side forces along a slender body of revolution at incidence. *Physical Review Fluids* 7, 124101 (2022), 2022. https://doi.org/10.1103/PhysRevFluids.7.124101.
- [11] Ma, Bao-F., Huang, Y. and Deng, X.-Y. Dynamic responses of asymmetric vortices over slender bodies to a rotating tip perturbation. *Exp. Fluids* (2016), 57:54. https://doi.org/10.1007/s00348-016-2139-3.
- [12] Mahadevan, S., Rodríguez, J. and Kumar. R. Effect of controlled imperfections on the vortex asymmetry of a conical body at high incidence. *35th AIAA Applied Aerodynamics Conference*, Denver, Colorado, USA, 2017. https://doi.org/10.2514/6.2017-3240.
- [13] Taligoski, J., Fernández, E., Uzun, A. and Kumar, R. Study of the roll orientation effects on vortex asymmetry on a conical forebody at high angles of incidence. *53rd AIAA Aerospace Sciences Meeting*, Kissimmee, Florida, USA, 2015. https://doi.org/10.2514/6.2015-0547.
- [14] Taligoski, J., Fernández, E. and Kumar, R. Experimental investigation of vortex asymmetry on a conical forebody at high angles of incidence. *52nd AIAA Aerospace Sciences Meeting*, National Harbor, Maryland, USA, 2014. https://doi.org/10.2514/6.2014-0051.
- [15] Taligoski, J., Uzun, A. and Kumar, R. Numerical investigation of vortex asymmetry on a conical forebody at high angles of incidence. *52nd AIAA Aerospace Sciences Meeting*, National Harbor, Maryland, USA, 2014. https://doi.org/10.2514/6.2014-0052.
- [16] Kumar, R., Guha, T. K. and Kumar, R. Role of secondary shear-layer vortices in the development of flow asymmetry on a cone-cylinder body at high angles of incidence. *Experiments in Fluids* (2020) 61:215, 2020. https://doi.org/10.1007/s00348-020-03045-y.
- [17] Wei, K., Chen, S., Xu, Y. and Tang, D. Influence of roughness on the asymmetric flow field of a slender body. *International Journal of Aerospace Engineering*, Vol 2022, 2022. https://doi.org/10.1155/2022/6590152.

- [18] Deane, J.R. An Experimental and theoretical investigation into the asymmetry vortex flow characteristics of bodies of revolution at high angles of incidence in low speed flow. *GARTEUR TP-109* (also BT 16482). Final Report of Group for Aeronautical Research and Technology in Europe GARTEUR-AG04, 1984.
- [19] Menter, F.R. and Egorov, Y. A scale adaptive simulation model using two-equation models. *43*rd *Aerospace Sciences Meeting and Exhibit*, Reno, Nevada, USA, 2005. https://doi.org/10.2514/6.2005-1095.
- [20] Menter, F.R. and Egorov, Y. The scale-adaptive simulation method for unsteady turbulent flow predictions. Part 1: Theory and model description. *Flow Turbulence Combustion (2010)* 85:113-138, June 2010. https://doi.org/10.1007/s10494-010-9264-5.
- [21] Menter, F.R., Schütze, J., Kurbatskii, K.A., Gritskevich, M. and Garbaruk, A. Scale-resolving simulation techniques in industrial CFD. 6th AIAA Theoretical Fluid Mechanics Conference, Honolulu, Hawaii, USA, 2011. https://doi.org/10.2514/6.2011-3474.
- [22] Menter, F.R., Kuntz, M. and Bender, R. A scale-adaptive simulation model for turbulent flow predictions. *41*st *Aerospace Sciences Meeting and Exhibit*, Reno, Nevada, USA, 2003. https://doi.org/10.2514/6.2003-767.
- [23] Egorov, Y., Menter, F.R., Lechner, R. and Cokljat, D. The scale-adaptive simulation method for unsteady turbulent flow predictions. Part II: Application to complex flow. *Flow Turbulence Combustion* (2010) 85:139-165, June 2010. https://doi.org/10.1007/s10494-010-9265-4.
- [24] ANSYS FLUENT. Theory guide, pp 92-95. Release 19.1. ANSYS, Inc., Southpointe 2600 ANSYS Drive. Canonsburg, PA 15317, USA, 2018.
- [25] Seifert, J. A review of the Magnus effect in aeronautics. *Progress in Aerospace Sciences* 55 (2012) 17-45, 2012. http://dx.doi.org/10.1016/j.paerosci.2012.07.001.
- [26] Nielsen, *J. Missile Aerodynamics*. Nielsen Engineering & Research Inc.: Santa Clara, CA, USA, 1988. ISBN 0-9620629-0-1.
- [27] Morote, J. and Liaño, G. Prediction of nonlinear rolling and Magnus coefficients of cruciform-finned missiles. *J. Aircraft* 2010, 47, 1413-1425, 2010. https://doi.org/10.2514/1.47212.
- [28] Liaño, G., Castillo, J.L. and García-Ybarra, P.L. Nonlinear model of the free-flight motion of finned bodies. *Aerosp. Sci. Technol.* 2014, 39, 315-324, 2014. https://doi.org/10.1016/j.ast.2014.10.001.
- [29] Liaño, G., Castillo, J.L. and García-Ybarra, P.L. Steady states of the rolling and yawing motion of unguided missiles. *Aerosp. Sci. Technol.* 2016, 59, 103-111, 2016. https://doi.org/10.1016/j.ast.2016.10.016.
- [30] Regan, F.J., Shannon, J.H.W. and Tanner, F.J. The joint NOL/RAE/WRE research Programme on bomb dynamics Part III. A low-drag Bomb with freely spinning stabilizers. *WRE Report-904* (WR&D), Department of Supply, Australian Defence Scientific Service, Salisbury, South Australia, 1973.
- [31] Gilbert, N.E. The Use of rate gyroscopes in the free flight measurement of aerodynamic lateral force and moment coefficients. *Technical Note HAS 164*, Department of Supply, Australian Defence Scientific Service, Salisbury, South Australia, 1973.
- [32] Dubief Y. and Delcayre, F. On coherent-vortex identification in turbulence, *Journal of Turbulence*, 2011, 1, N11, 2011. https://dpi.org/10.1088/1468-5248/1/1/011.
- [33] Holmén, V. Methods for vortex identification, Ph D Thesis, November 2012.
- [34] Bhagwandin, V. Numerical prediction of roll damping and Magnus dynamic derivatives for finned projectiles at angle of attack. *30th AIAA Applied Aerodynamics Conference*, AIAA 2012-2905, New Orleans, LA, USA, 25-28 June 2012. https://doi.org/10.2514/6.2012-2905.
- [35] Eidell, M.R., Nance, R.P., McGowan, G. Z., Carpenter, J.G. and Moore, F.G. Computational investigation of roll damping for missile configuration. *30th AIAA Applied Aerodynamics Conference*, New Orleans, LA, USA, 2012. https://doi.org/10.2514/6.2012-2904.
- [36] Jiménez-Varona, J. Numerical analysis of the Magnus effect on the forces past an axisymmetric body at high incidence. *Aerospace (2023)*, 10, 163, 2023. https://doi.org/10.3390/aerospace10020163.
- [37] Prananta, B.B., Deck, S., d'Éspiney, P., Jirasek, A., Kovak, A., Leplat, M., Nottin, C., Petterson, K. and Wrisdale, I. Numerical simulation of turbulent and transonic flows about missile configurations, *Final Report GARTEUR (AD) AG42 Missile Aerodynamics*, Group for Aeronautical Research and Technology in Europe (GARTEUR), 2007, Tech. Report. NLR-TR-2007-704.
- [38] Shaw S., Anderson, M., Barakos, G., Boychev, K., Dikbaş, E., DeSpirito, J., Loupy, Gaetan L., Schnepf, C. and Tormalm, M. The influence of modelling in prediction of vortex interactions about a generic missile airframe: RANS. AIAA SCITECH 2022 Forum, San Diego, CA, USA, 2022. https://doi.org/10.2514/6.2022-0416